6-2013

Multi-Dimensional Modeling Pyrolysis Gas Flow inside Charring Ablators

Haoyue Weng
University of Kentucky, kimomt@gmail.com

Alexandre Martin
University of Kentucky, alexandre.martin@uky.edu

Multi-Dimensional Modeling Pyrolysis Gas Flow inside Charring Ablators

Digital Object Identifier (DOI)
http://dx.doi.org/10.2514/6.2013-2635

Notes/Citation Information
Published in the *Proceedings of the 44th AIAA Thermophysics Conference*, Paper 2013-2635, p. 1-17.

Fluid Dynamics and Co-located Conferences
June 24-27, 2013, San Diego, CA
44th AIAA Thermophysics Conference

Multi-dimensional modeling pyrolysis gas flow inside charring ablators

Haoyue Weng* and Alexandre Martin†
University of Kentucky, Lexington, KY, 40506, USA

Using an ablative thermal/material response code, the importance of three-dimensionality for modeling ablative test-article is addressed. In particular, the simulation of the pyrolysis gas flow inside a porous material is presented, using two different geometries. The effects of allowing the gas to flow out of the side wall are especially highlighted. Results show that the flow inside the test-article is complex, and that the 0D or 1D assumption made in most Material Response (MR) codes might not be valid for certain geometries.

I. Introduction

DURING an atmospheric entry/re-entry, when a spacecraft travels at hypersonic speed, a strong bow shock is formed in front of the entering vehicle. Such a shock results in an enormous amount of aerodynamic heat, part of which is transferred to the thermal protection system (TPS). Of the many TPS options, charring ablators have gained popularity in recent years for their effectiveness and light weight. They are made of a fibrous non-pyrolyzing matrix (usually carbon or silicon carbide) and impregnated with pyrolyzing material (often phenolic resin). Phenolic Impregnated Carbon Ablator (PICA), as used for the MSL and the Stardust missions, is one such kind of material.[1] The idea behind this type of material is to dissipate part of the energy through pyrolysis and ablation. Pyrolysis is the process in which the phenolic polymer gradually carbonizes at high temperature, losing mass and generating pyrolysis gases. These gases are then expelled through the porous structure of the material and blown into the chemical reacting boundary layer. The other phenomenon, surface ablation, refers to the mass removal of the char (composed of non-pyrolyzed and residual carbonized material) through oxidation, sublimation and spallation.

Much research has been done on this topic. However, most of the simulation tools available in the literature are one or two-dimensional.[2–6] Admittedly, a one-dimensional solution is mostly adequate for design purposes; for predictive analysis, however, it might not be sufficient to take into account all phenomena taking place inside the charring ablator. For example, materials like PICA possess orthotropic properties. The thermal conductivity in the "in-plane" direction is significantly higher than in the "through-the-thickness" direction. Thus, the one-dimensional response models usually underestimate the centerline temperature rise.[7] Similarly, the permeability of PICA material is higher in the "in-plane" than in the "through-the-thickness" direction, which is in accord with the anisotropic microstructure of the carbon fiber matrix.[8] If the pyrolysis gases blowing rate along a curved surface is concerned, a one-dimensional model might not be accurate.

But more importantly, it has been hypothesize that surface mass fluxes are greatly influenced by the geometry of the material tested.[9] This is of great importance when small test-articles are employed to derive and validate models that are used in very different geometrical configurations. For instance, as it is not feasible to fit an entire heat-shield in ground tests facilities such as arc-jets or ICP torches, samples of a few inches are being used for validation and model calibration.[10–17]

Most ablation code, if not all, use simple analysis for the gas transport; the pyrolysis gas is either assumed to instantly exit at the surface (0D assumption), or simply travel along a normal line (1D assumption). In this research effort, the multi-dimensionality behavior of the pyrolysis gas inside samples are presented. Using samples comparable to the ones used in ground testing facilities, it is shown that those assumption

*Graduate Research Assistant, Department of Mechanical Engineering, AIAA Student Member
†Assistant Professor, Department of Mechanical Engineering, Associate Faculty – Center for Computational Science, AIAA Senior Member

are not necessarily valid, and that the geometrical effects are non-negligeable. Although more validations are needed, the present analysis clearly demonstrates the need for three-dimensional calculations.

II. Numerical Framework

The Material Response (MR) solver is build using a the general computing framework KATS currently being developed at the University of Kentucky.[18,19] The code uses the popular CGNS format for the computational grid and takes advantage of parallel computing through domain decomposition (ParMETIS) and MPI. To solve the large sparse linear system, the code is linked to the PETSc library.

The governing equation solved in the code have the following general form:

$$\frac{\partial \mathbf{Q}}{\partial t} + \nabla \cdot (\mathbf{F} - \mathbf{F_d}) = \mathbf{S}, \tag{1}$$

where $\mathbf{Q}$ is the vector of conservative variables, $\mathbf{F}$ and $\mathbf{F_d}$ are respectively convective and diffusive face flux, and $\mathbf{S}$ is the source term in general.

Taking a second order finite volume approach and fully implicit backward Euler time integration, the above equation becomes

$$\left[\frac{V}{\Delta t}\frac{\partial \mathbf{Q}}{\partial \mathbf{P}} - \frac{\partial \mathbf{R}}{\partial \mathbf{P}}\right]\Delta \mathbf{P} = \mathbf{R}, \tag{2}$$

where V is the volume of the cell, Δt the time step, and $\mathbf{P}$ is the primitive variables vector. The right hand side of the equation, represented by $\mathbf{R}$, is defined as

$$\mathbf{R} \equiv -\sum_{\text{faces}} (\mathbf{F} - \mathbf{F_d}) \cdot \mathbf{n} A + \mathbf{S} V \tag{3}$$

where A is the face area and $\mathbf{n}$ is the face normal direction. Note that Eq. (2) directly solves the update of primitive variables, which are usually physical quantities. Therefore, the physical variables are readily available and used for updates, while preserving a conservative formulation.

III. Proposed models

The Material Response (MR) code developed in this work solves gaseous and solid mass, momentum and overall energy equations. The governing equations, in the context of Eq. (1) and (2), can be represented by the following vectors and matrices.

$$\mathbf{Q} = \begin{pmatrix} \phi\rho_g \\ \rho_{s1} \\ \vdots \\ \rho_{sns} \\ \phi\rho_g u \\ \phi\rho_g v \\ \phi\rho_g w \\ \phi E_g + E_s \end{pmatrix}, \qquad \mathbf{P} = \begin{pmatrix} \phi\rho_g \\ \rho_{s1} \\ \vdots \\ \rho_{sns} \\ u \\ v \\ w \\ T \end{pmatrix}, \qquad \mathbf{S} = \begin{pmatrix} \omega_g \\ \omega_{s1} \\ \vdots \\ \omega_{sns} \\ D_x \\ D_y \\ D_z \\ S_D \end{pmatrix}, \tag{4}$$

$$\mathbf{F} = \begin{pmatrix} \phi\rho_g u & \phi\rho_g v & \phi\rho_g w \\ 0 & 0 & 0 \\ \vdots & \vdots & \vdots \\ 0 & 0 & 0 \\ \phi\rho_g u^2 + p & \phi\rho_g vu & \phi\rho_g wu \\ \phi\rho_g uv & \phi\rho_g v^2 + p & \phi\rho_g wv \\ \phi\rho_g uw & \phi\rho_g vw & \phi\rho_g w^2 + p \\ \phi\rho_g uH & \phi\rho_g vH & \phi\rho_g wH \end{pmatrix}, \qquad \mathbf{F_d} = \begin{pmatrix} 0 & 0 & 0 \\ 0 & 0 & 0 \\ \vdots & \vdots & \vdots \\ 0 & 0 & 0 \\ & & \\ & \mathbf{0} & \\ & & \\ & F_{cond} & \end{pmatrix}. \tag{5}$$

Here, the pyrolysis gases are assumed to be in chemical equilibrium, and are therefore modeled as one single entity. Thus, there is only one equation for the mass conservation of pyrolysis gas. Note that the properties of pyrolysis gas (*e.g.* viscosity, heat capacity, enthalpy, etc.) are obtained from equilibrium table. ϕ is porosity, which is modeled as a function of total solid density. For solid species, a phenomenological three-component model is used.[4] The total solid density is therefore computed using

$$\rho_s = \sum_{i=1}^{3} \Gamma_i \rho_{si}, \tag{6}$$

where Γ_i is the volume fraction of species i in the virgin composite. Since it is impossible to measure the material properties during charring process, the intermediate state is interpolated from the virgin and char states. The solid decomposition rate of each component can be evaluated by performing a temporal derivative of Eq. (6)

$$\frac{\partial \rho_s}{\partial t} = \sum_{i=1}^{3} \Gamma_i \frac{\partial \rho_{si}}{\partial t}. \tag{7}$$

The decomposition rate of each constituent is given by

$$\omega_{si} = \frac{\partial \rho_{si}}{\partial t} = -A_i \rho_{vi} \left(\frac{\rho_{si} - \rho_{ci}}{\rho_{vi}} \right)^{\psi_i} \exp\left(\frac{-E_i}{RT} \right), \qquad T > T_{react_i}, \tag{8}$$

where subscript v and c are respectively for the virgin and charred states of the solid material. The solid decomposition and pyrolysis gas generation balance themselves, thus ensuring total mass conservation:

$$\omega_g = -\sum_{i=1}^{3} \Gamma_i \omega_{si}. \tag{9}$$

Flow through porous medium

Flow through porous medium is often modeled with Darcy's law.[20] In this work, the gas momentum is solved as distinct momentum conservation in the governing equations. The diffusive effect of porous media is treated as a source term in each direction of the equation, that is D_x, D_y, and D_z, as depicted in Eq. (4). These terms, in general, may be calculated by solving the following linear equation:

$$\begin{pmatrix} K_{xx} & K_{xy} & K_{xz} \\ K_{yx} & K_{yy} & K_{yz} \\ K_{zx} & K_{zy} & K_{zz} \end{pmatrix} \begin{pmatrix} D_x \\ D_y \\ D_z \end{pmatrix} = -\phi\mu(1 + Fo) \begin{pmatrix} u \\ v \\ w \end{pmatrix}, \tag{10}$$

where Fo is Forcheimer number which accounts for high velocity effects at the pore scale. The 3 by 3 matrix on the left hand side is the anisotropic tensor of solid permeability. It is to be noted that, using this formulation, if the flow is steady, and that the Forcheimer number is very small, the whole momentum equation simply becomes Darcy's Law. Finally, as is the case with the viscous momentum fluxes, the viscous energy fluxes are moved to the source term, and are given by $S_D = uD_x + vD_y + wD_z$. In this present work, however, this source term is neglected.

Conductive heat transfer

The conductive heat flux, as appeared in $\mathbf{F_d}$ of Eq. (5), is also given in a general anisotropic fashion as following:

$$F_{cond} = \begin{pmatrix} k_{xx} & k_{xy} & k_{xz} \\ k_{yx} & k_{yy} & k_{yz} \\ k_{zx} & k_{zy} & k_{zz} \end{pmatrix} \begin{pmatrix} \partial T/\partial x \\ \partial T/\partial y \\ \partial T/\partial z \end{pmatrix}. \tag{11}$$

IV. Test Cases Description

IV.A. Material model

The material model use to perform the simulation presented below is known as TACOT (Theoretical Ablative Composite for Open Testing).[21] TACOT, a low-density theoretical carbon ablator, has similar properties to the PICA;[1] most importantly, it has a very comparable porosity and permeability. The charring process of TACOT is modeled with a phenomenological three-component decomposition model, thus giving three solid mass balance equations and a total of eight equations to solve. For results presented here, in an attempt at simplifying as much as possible the problem, all material properties are isotropics.

IV.B. Geometry and boundary conditions

The first test case presented is a direct extension of the 1D assumption to 3D. The geometry is therefore a cylindrical shape test piece. The mesh used for this run is presented in Fig. 1. The diameter and the height of the cylinder are both 10 centimeters. The top surface is subjected to a uniform heat for 40 seconds, at which point the heat is removed. The bottom wall and the side wall, in this case, are adiabatic and impermeable. The pressure boundary condition is set to be constant.

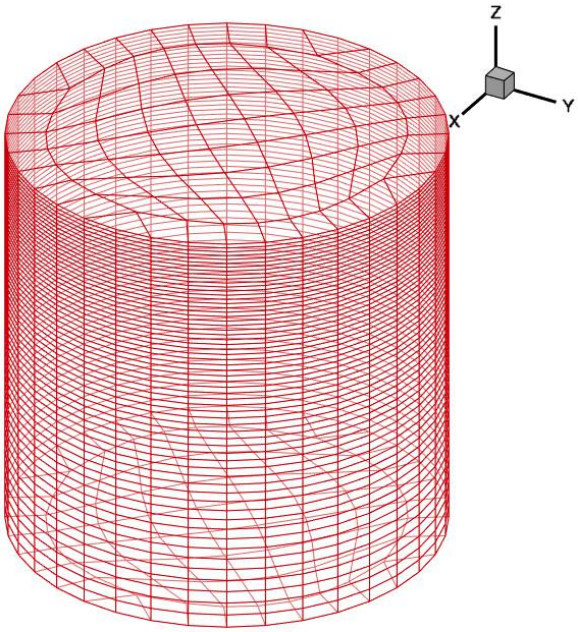

Figure 1. Grid used for Case 1 and Case 2

The second test case is identical to the first one, with the sole exception that the side wall is permeable. Therefore, the pyrolysis gases are free to move in and out through the side wall boundary.

The third test case uses a slightly modified version of the Iso-Q geometry as a geometry, proposed by van Eeckelen et. al.[22] In this adapted version, the top surface, the one exposed to the heat flux, is represented by an ellipse arc. Figure 2 shows the sizes of cylinder and Iso-Q shape used in all of the test cases. Since the problem is axisymmetric, the simulation is performed in two-dimensional. The mesh for Case 3 is depicted in Fig. 3: both sides of the symmetry axis are shown, for illustrative purposes. The non uniform heat flux, illustrated in Fig. 4, is obtained through a CFD simulation.[22] Again, the heat is removed after 40 seconds. The pressure however, is uniform in this case.

The fourth test case is identical to the third, although the side wall is now impermeable. It uses the same geometry, mesh and applied heat flux as in third test case.

The fifth test case explores the effect of non-uniform pressure boundary condition. The pressure distribution shown in Fig. 4 is applied, in addition to the heat flux distribution. Also, a 20-second linear ramping is used to prevent the atmospheric gas from being immediately pulled out through the sample, which causes numerical problems. The ramping of both heat flux and pressure are presented in Fig. 5.

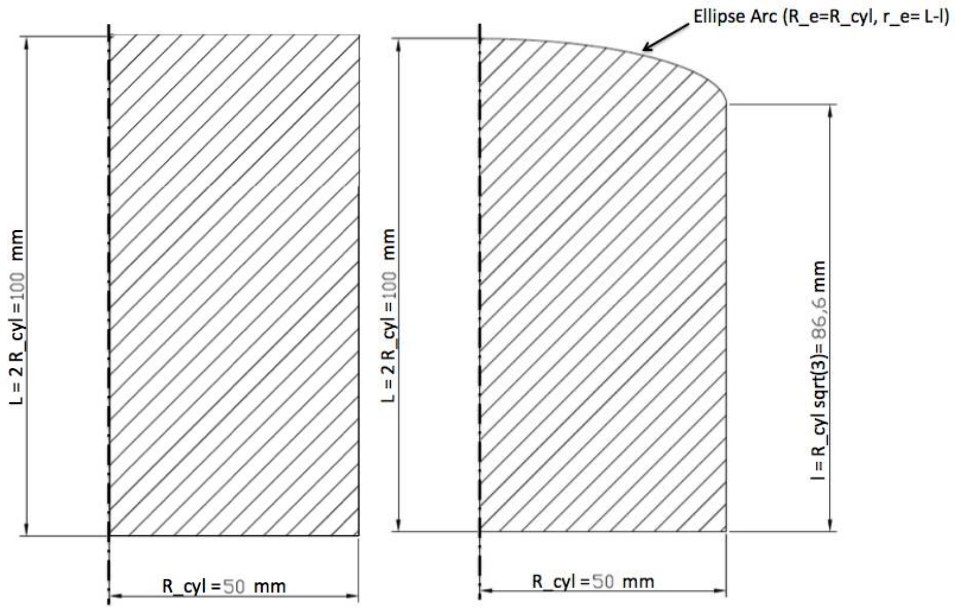

(a) Cylinder (b) Iso-Q

Figure 2. Geometry of the cylinder and the Iso-Q shape (from Ref. 22)

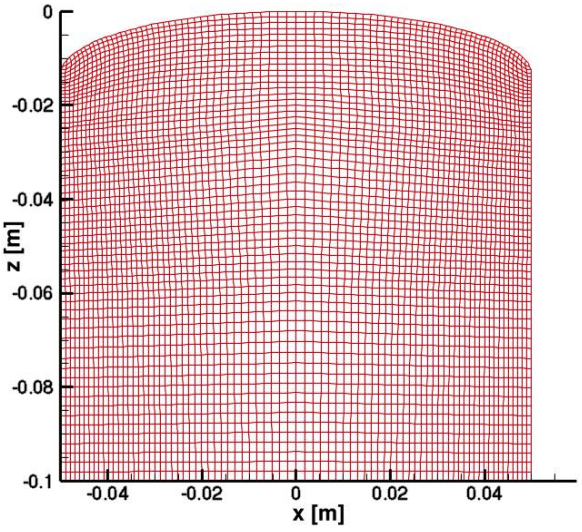

Figure 3. Grid used for Test Case 3 and Case 4

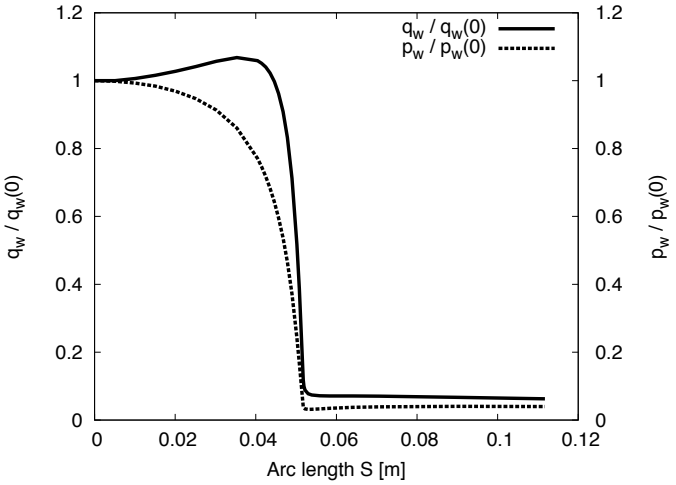

Figure 4. Heat flux and pressure distribution (from Ref. 22)

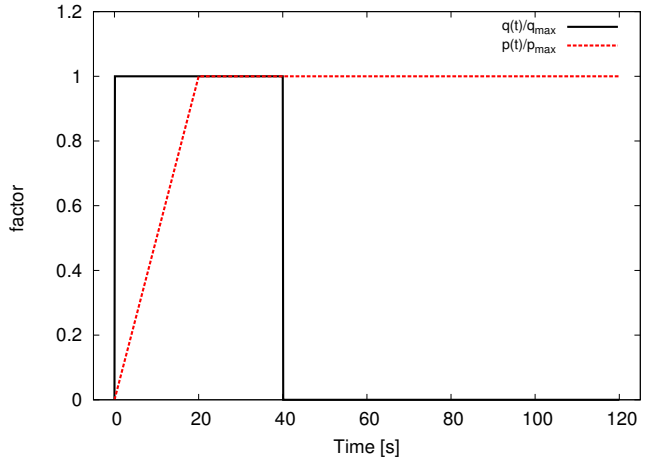

Figure 5. Heat flux and pressure boundary conditions ramping

V. Results, Comparisons and Discussions

V.A. Side wall effects

To demonstrate the pyrolysis gas flow behavior, streamline curves are used as indication of the flow patterns. The contours of $\dot{m}'' = \phi\rho_g|\mathbf{V}|$ are also plotted to provide momentum transport information. For the first two test cases, the streamline plots taken at the $y = 0$ slice are presented in Fig. 6 for 20 sec, 40 sec, and 60 sec. Notice that the streamlines are significantly different in these two cases. The streamlines in the first test case are all straight and parallel, pointing upwards. This indicates the pyrolysis gas only blows from the front. This is analogues to one-dimensional models and results, since the equation set used to represent the pyrolysis gas momentum is Eulerian-type, using which the wall boundary condition is slip (this is, of course, a sound assumption for porous media, as the non-slip occurs at the surface of the pores, not at the surface of the test-piece). As a result, the simulation of Case 1 should be, and is, exactly the same as a 1D case. In Case 2, where the side walls are permeable, the streamline shows strong blowing through the side walls. The portion of gas momentum blowing through front is small in scale compared with the amount that leaves from the sides.

The difference in the pressure distribution for these two test-cases are presentend on Fig. 7. As expected, the pressure for Case 1 (left) is identical to the one computed using 1D codes. However, the pressure distribution for the case of the impermeable side is very different. As the pyrolysis gas is formed, instead of being pushed up and down, the gas immediately leaves the samples from all sides. This prevent the pressure build up, and therefore, gas mass accumulation.. This behavior therefore clearly contradict the 1D assumption usually made in most MR code.

Figure 8 shows the normal mass flux, defined as $\dot{m} = \phi\rho_g\mathbf{V}\cdot\mathbf{n}$, over surface length of the test specimen geometry of Case 1 and Case 2. As can be clearly seen from Fig. 8(b), the highest pyrolysis gases mass blowing point is on the side, instead of the front. The mass flux blowing from the front is considerably less significant than from the side, especially considering the total mass flux is the surface integral of the cylindrical-like shape. For the 1D model, represented in Fig. 8(a), the largest and only amount of mass flux is from the front, because all side blowing effects are inherently neglected due to lack of dimensions.

For the Iso-Q cases, namely Case 3 and Case 4, even more geometry effect are taken into account. Similarly to the previous sets, $\dot{m}''$ contour plots with streamlines are presented in Fig. 9.

The plots on the left, which corresponds to the results using permeable side, are again very different then the impermeable side case on the right. As is shown in Fig. 9(c), a strong momentum transport layer takes place right below the charring front. This transport shows the pyrolysis gas goes inside of the material and rounds toward the sides, since the back wall is still impermeable. For the impermeable case, the streamlines in Fig. 9(b), 9(d) and 9(f) show that the pyrolysis gases flux can only exit at the ellipse curve front. Even though the profile is generally flat, there is a peak on the outer ring of the Iso-Q geometry, indicating the gas mass flows through the two ends of the geometry. This can also be implied by Fig. 11, in which surface mass flux are displayed for Case 3 and Case 4.

Fig. 10 shows the pressure distribution inside the test-samples. As expected, the impermeable side causes a pressure buildup inside the sample, as was the case with the cylinder.

Figure 11(a) clearly shows the highest $\dot{m}$ takes place on the sides, not front. In particular, the peak pyrolysis mass flux is located right below the shoulder region, and it quickly tails down as the side wall goes to the end. The behavior of impermeable side case, however, is completely different. It starts from a relative flat blowing mass flux at the front, decreases slightly and as it reaches the end of Iso-Q curve, increases tremendously. Taking the surface integral of the mass flux along the geometry yields the mass blowing rates from front and side, as is shown in Table 1. For the permeable side Iso-Q case, more than 50% of the mass blows from the side. This percentage increases to more than 70% at 40 seconds. In the case of the impermeable side, as expected, all of the gases can only flow through the front. Also note that comparing only the mass flux on the front surface, the values of blowing mass flux is still higher in the permeable side case. The reason for this behavior is not quite understood yet, and is most probably caused by combined effect on pressure, temperature, pyrolysis front velocity and pyrolysis gas generation. The impermeable case is intuitively expected to blow more due to the pressure build up, but the results are actually the opposite. As can be seen on Fig. 11(b), the mass flux is low from L =0 to 0.045, and then climbs up from about 0.045 to the end. When integrating this curve, however, the $L = [0, 0.045]$ domain consist of most of the surface area; the high max flux region is only integrated over a very narrow surface "ring", thus making the overall integral less than permeable case. Also, when looking at the charring front of the two cases, the charring

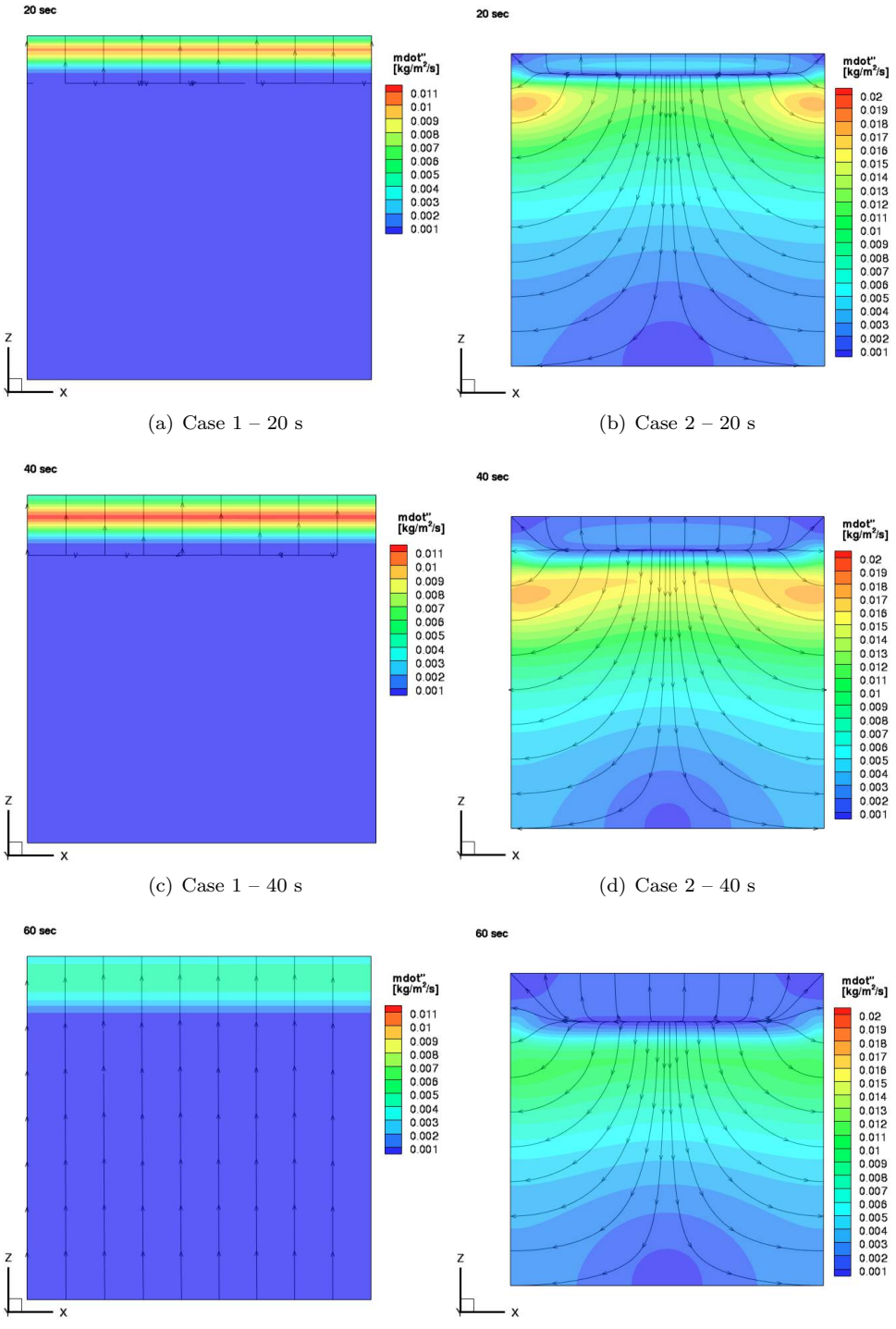

(a) Case 1 – 20 s

(b) Case 2 – 20 s

(c) Case 1 – 40 s

(d) Case 2 – 40 s

(e) Case 1 – 60 s

(f) Case 2 – 60 s

Figure 6. Inner mass flux distribution and stream lines for the cylindrical test-articles (Case 1, impermeable side, and Case 2, permeable side)

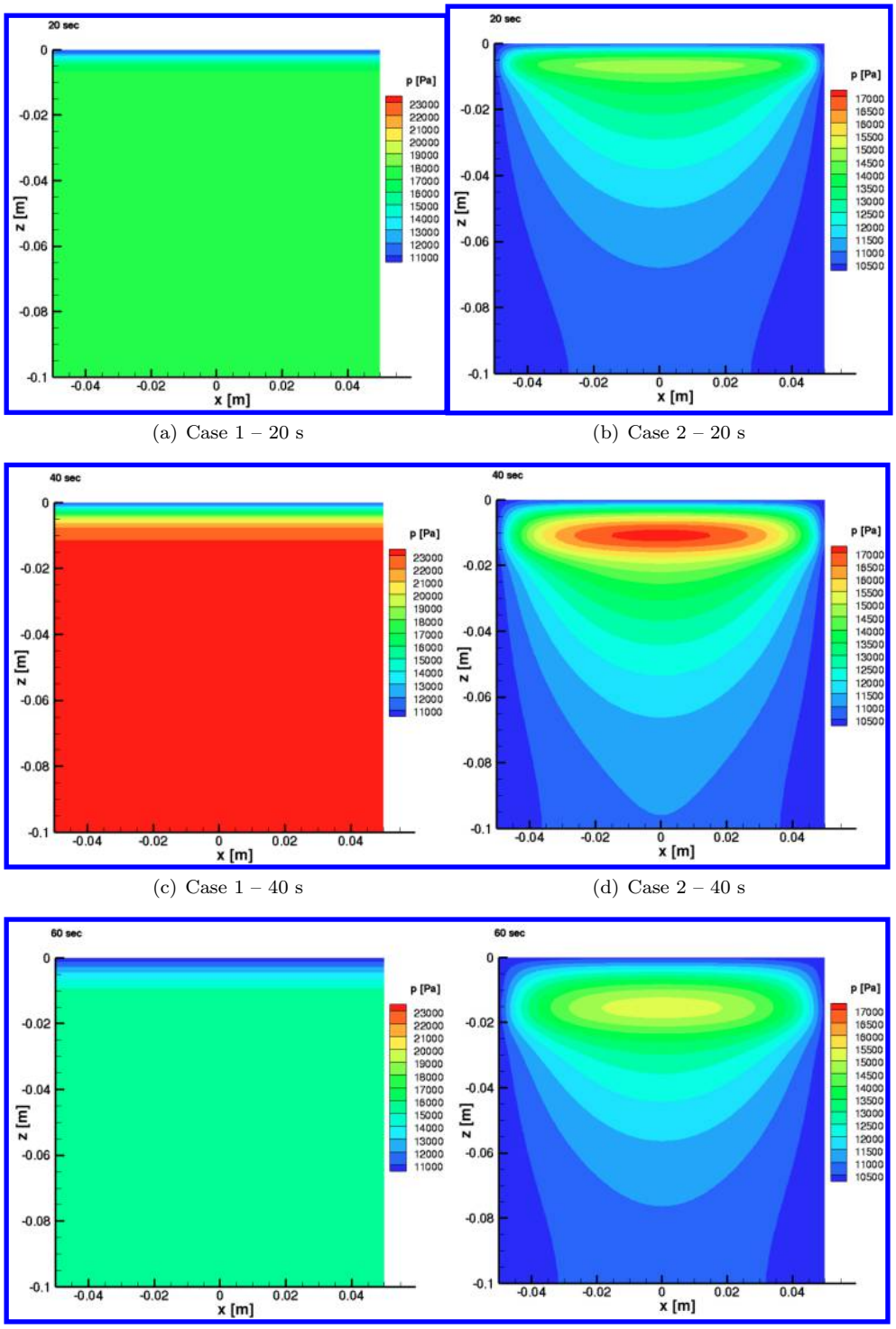

(a) Case 1 – 20 s (b) Case 2 – 20 s

(c) Case 1 – 40 s (d) Case 2 – 40 s

(e) Case 1 – 60 s (f) Case 2 – 60 s

Figure 7. Pressure distribution for the cylindrical test-articles (Case 1, impermeable side, and Case 2, permeable side)

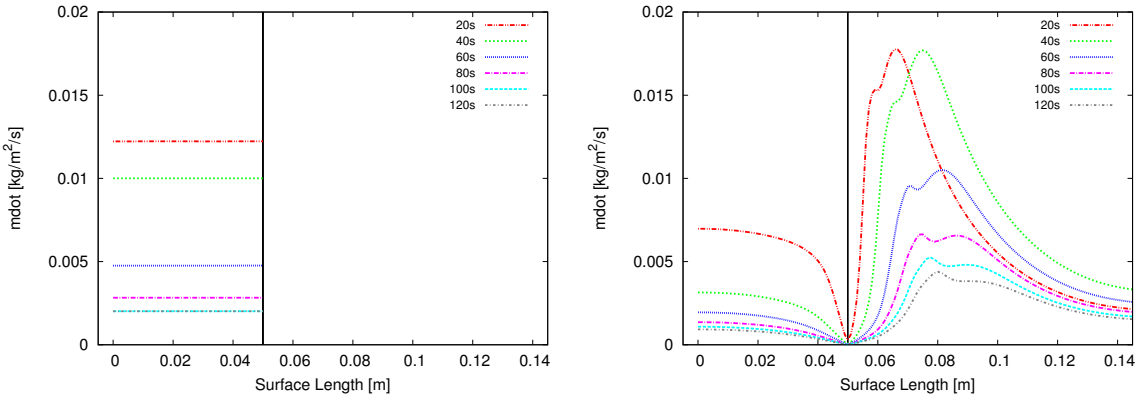

(a) Case 1 – Cylinder, impermeable side

(b) Case 2 – Cylinder, permeable side

Figure 8. Surface normal blowing mass flux for Case 1 and Case 2; the black line indicates the separation between the front surface, to the left, and the side surface, to the right

Table 1. Comparison of the mass rate leaving from the side and from the top, for Case 3 and Case 4

	Iso-Q, permeable side		Iso-Q, impermeable side	
Blowing	Front	Side	Front	Side
20s	2.72×10^{-3} (44.6%)	3.37×10^{-3} (55.4%)	1.06×10^{-4} (100%)	0
40s	1.99×10^{-3} (28.1%)	5.08×10^{-3} (71.9%)	8.66×10^{-5} (100%)	0
60s	1.25×10^{-3} (27.8%)	3.24×10^{-3} (72.2%)	4.27×10^{-5} (100%)	0
80s	7.94×10^{-4} (26.0%)	2.26×10^{-3} (74.0%)	2.57×10^{-5} (100%)	0
100s	5.67×10^{-4} (23.9%)	1.8×10^{-3} (76.1%)	1.85×10^{-5} (100%)	0
120s	4.43×10^{-4} (22.5%)	1.53×10^{-3} (77.5%)	1.46×10^{-5} (100%)	0

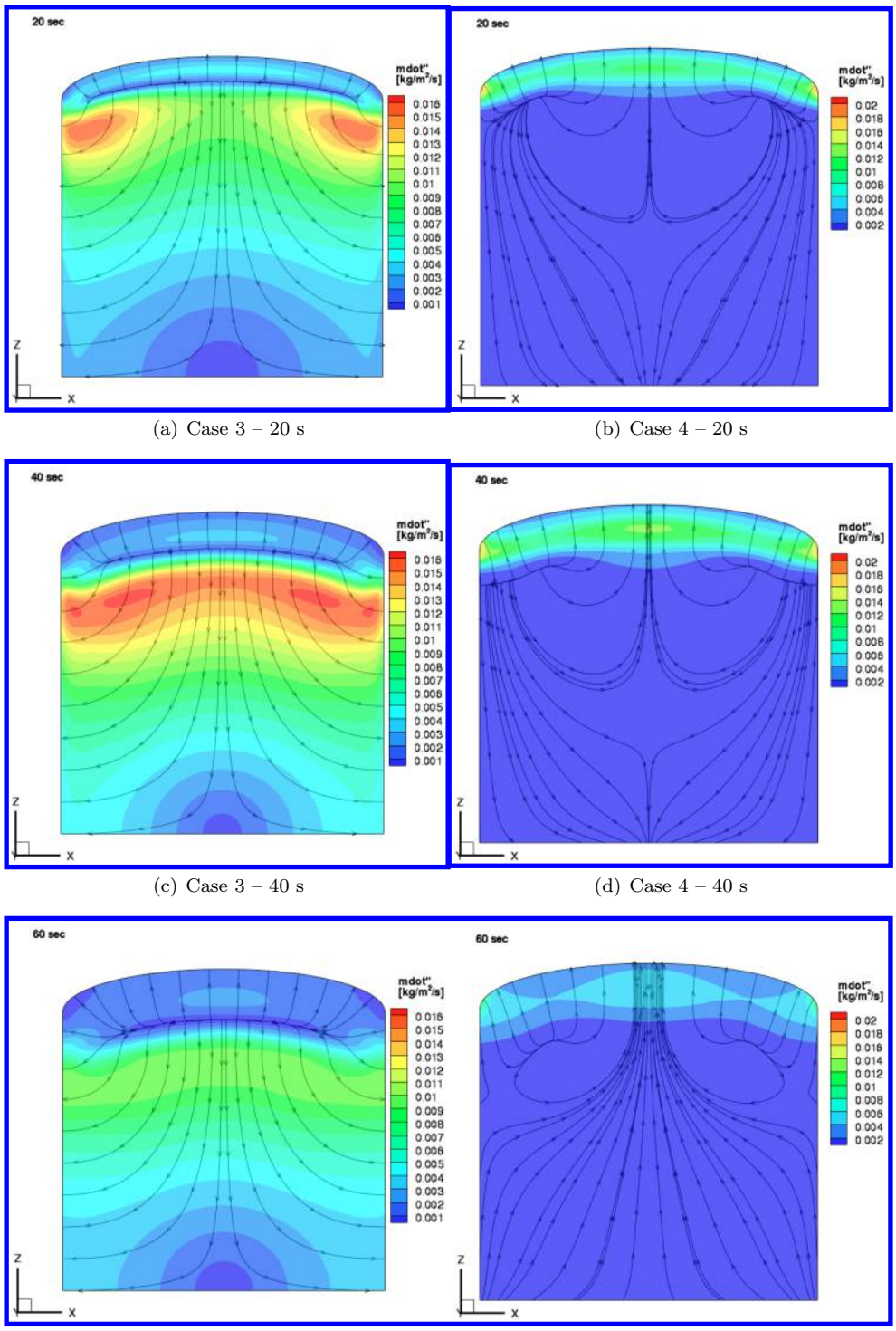

(a) Case 3 – 20 s

(b) Case 4 – 20 s

(c) Case 3 – 40 s

(d) Case 4 – 40 s

(e) Case 3 – 60 s

(f) Case 4 – 60 s

Figure 9. Inner mass flux distribution and stream lines for the Iso-Q test-articles (Case 3, permeable side, and Case 4, impermeable side)

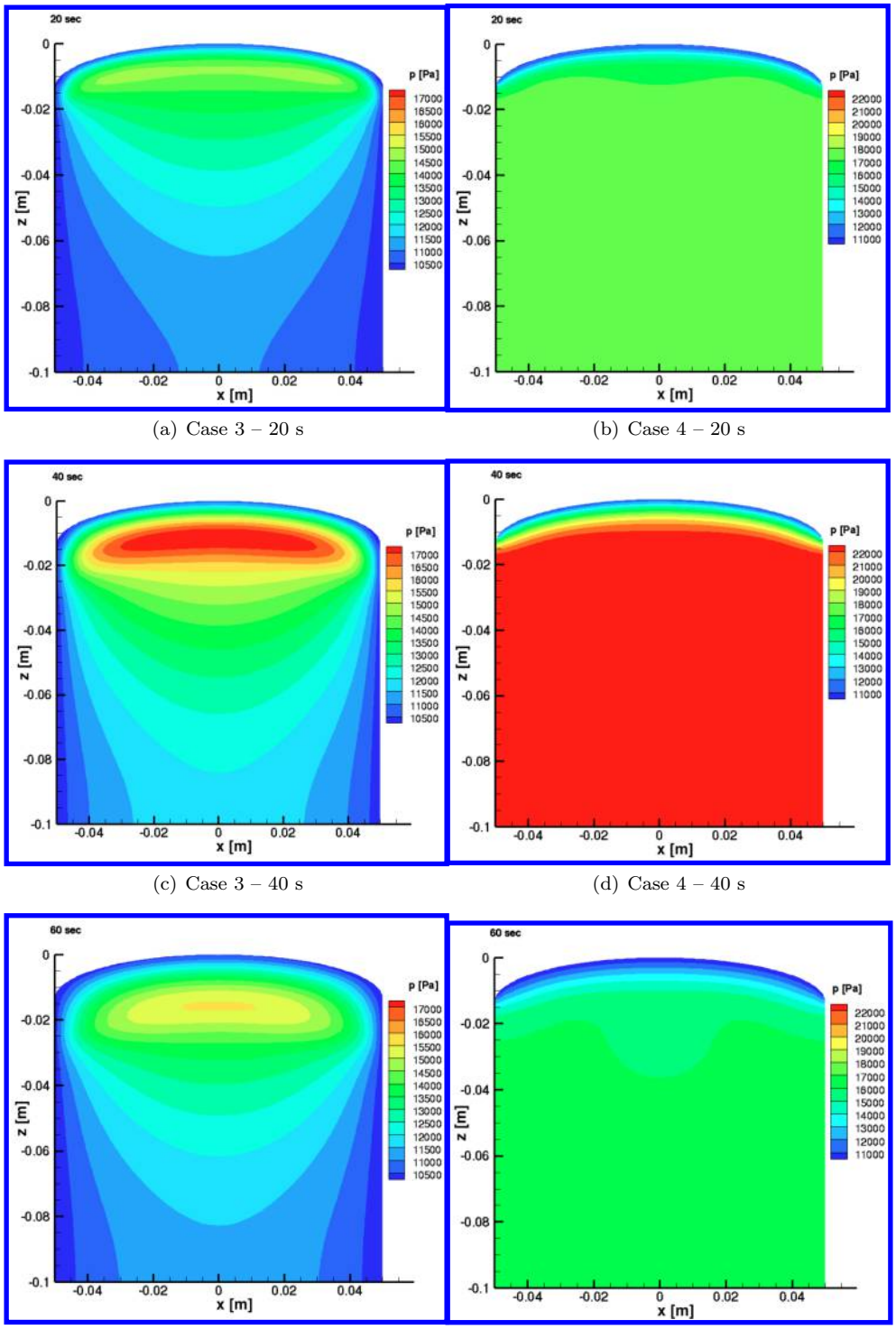

(a) Case 3 – 20 s (b) Case 4 – 20 s

(c) Case 3 – 40 s (d) Case 4 – 40 s

(e) Case 3 – 60 s (f) Case 4 – 60 s

Figure 10. Pressure distribution for the Iso-Q test-articles (Case 3, permeable side, and Case 4, impermeable side)

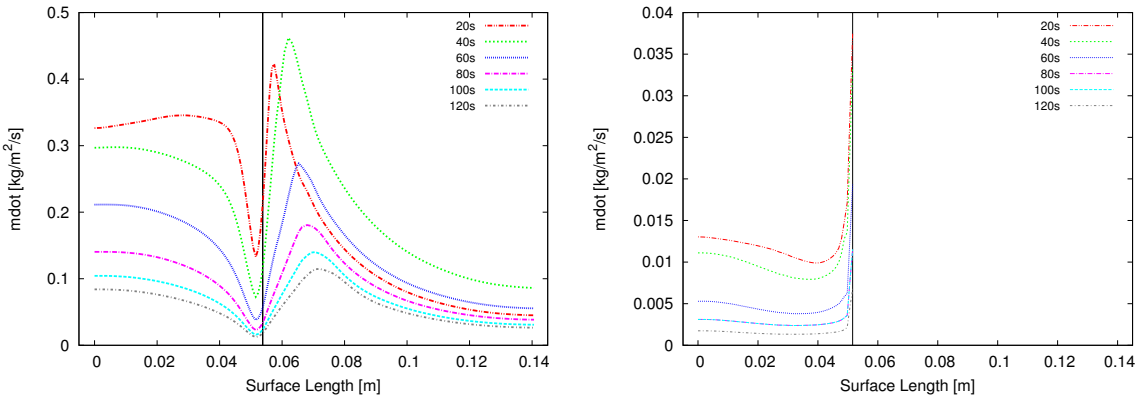

(a) Case 3 – Permeable side

(b) Case 4 – Impermeable side

Figure 11. Surface normal blowing mass flux for Case 3 and Case 4; the black line indicates the separation between the front surface, to the left, and the side surface, to the right

layer of permeable case is thicker than the impermeable one. This leads to more pyrolyzing and therefore more gas is generated (although it is not necessarily blowing at the front surface).

V.B. Effect of non-uniform pressure boundary condition

The effect of non-uniform pressure boundary condition is explored by comparing the results of Case 3 and Case 5. The mass flux isocontours with streamline are presented in Fig. 12. As for the pressure distribution, presented on Fig. 13, Case 5 is relatively similar to Case 3, apart from the fact that the variable pressure on the side causes difference within the depth of the sample.

It is to be noted that in Case 5, the pyrolysis gas momentum transport near shoulder region is slightly higher than in Case 3 and the blowing through the front is further weakened. This is because the pressure distribution tends to drive the pyrolysis gas from the front to the side if there is no in-depth decomposition. Also, due to this pressure boundary condition, the behavior of the blowing mass flux on the surface is quite interesting, as depicted in Fig. 14. The blowing mass flux is oscillating on the front surface and there is even atmospheric gas intake near the shoulder region of the geometry. Moreover, the mass flux is roughly an order of magnitude lower than Case 3.

This exploratory result clearly shows the importance of pressure distribution on the boundary. However, it is not trivial to fully investigate its behavior without accounting for the surrounding (boundary-layer) flow field interaction. Therefore, a fully coupled approach, where the atmospheric flow field is considered and calculated, is more likely needed.

VI. Summary and Conclusion

A three-dimensional material response code has been developed and tested on various geometry. Results have shown the capability of solving different three-dimensional charring ablative problems. Specifically, the pyrolysis gas flow inside of the charring ablative material is extensively considered. As expected, the mass flux at the surface is significantly different between 1D and multi-dimensional models. Instead of blowing from the front surface, the majority of gas mass flow goes through the side wall. For Iso-Q models, even if the wall is impermeable, most of the gases leave the sample from the side, due to the geometry effects. Therefore, the boundary layer effects in arc-jets might be different than currently assumed, and this effect becomes more important in smaller samples. Moreover, samples with impermeable side wall might not be able to correctly reproduce the interactions between the pyrolysis gas and the solid matrix while traveling inside the ablators.

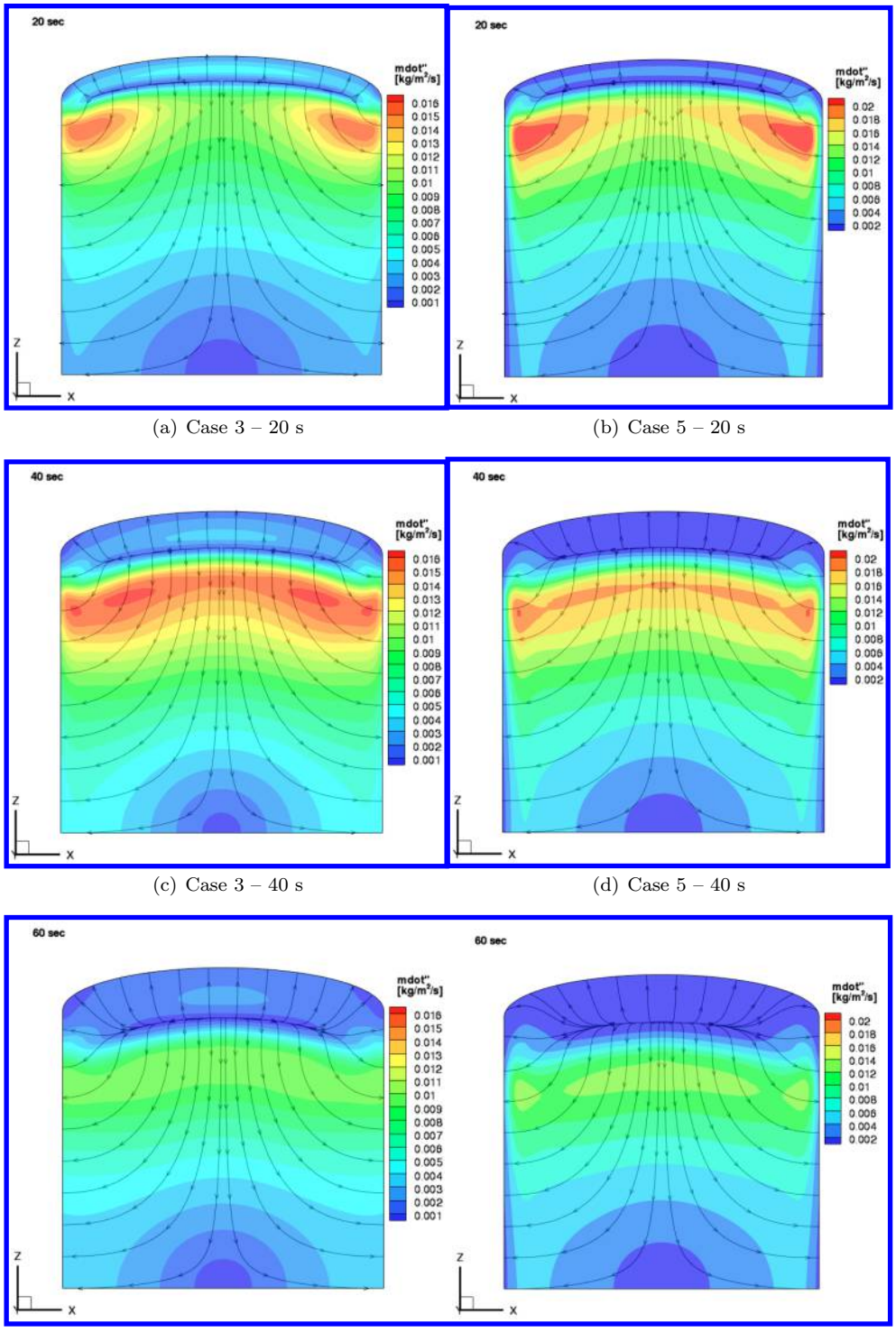

(a) Case 3 – 20 s

(b) Case 5 – 20 s

(c) Case 3 – 40 s

(d) Case 5 – 40 s

(e) Case 3 – 60 s

(f) Case 5 – 60 s

Figure 12. Inner mass flux distribution and stream lines for the Iso-Q test-articles using a non-uniform pressure distribution (Case 5) – for clarity, the results are compared to Case 3

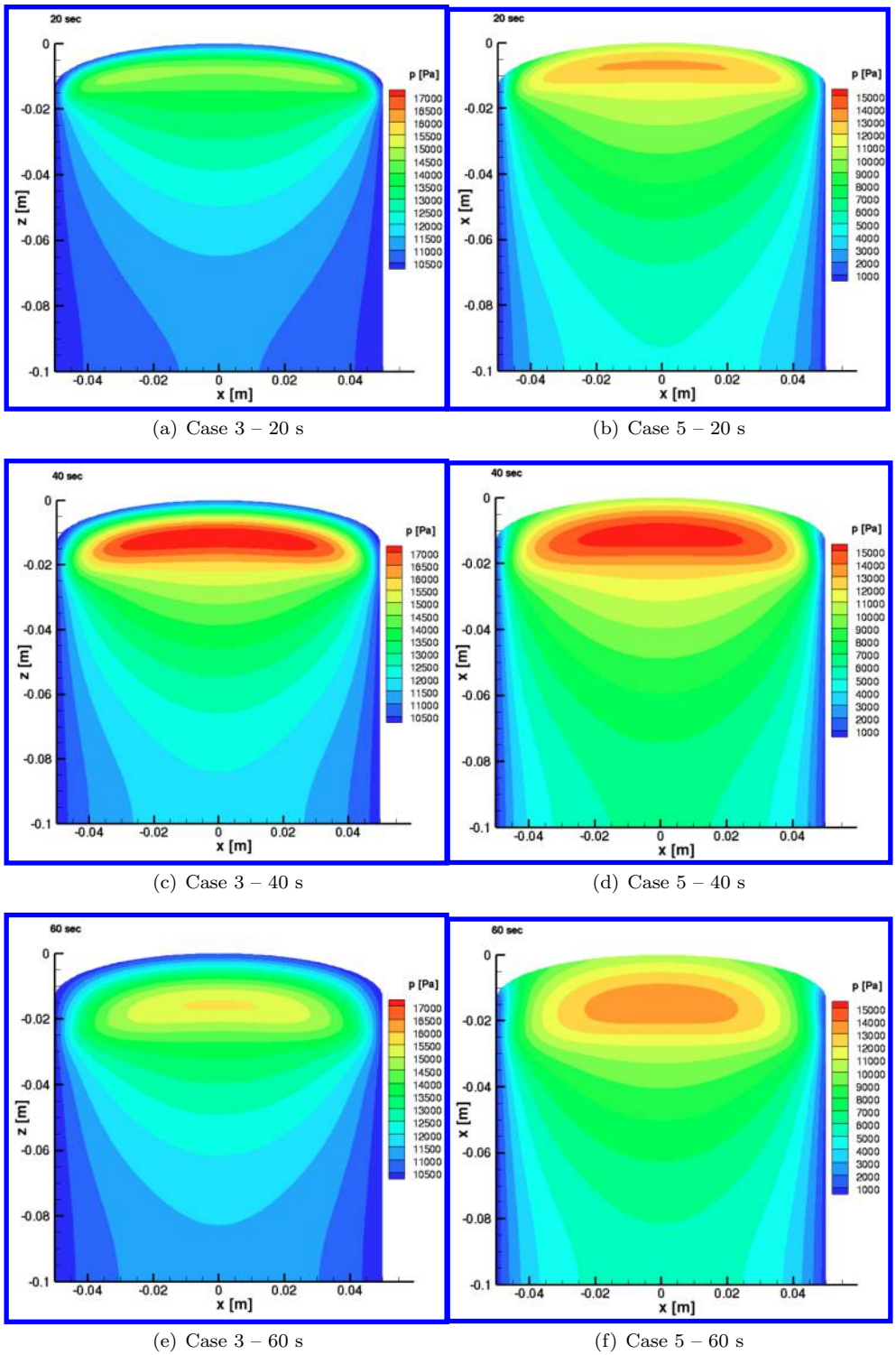

(a) Case 3 – 20 s

(b) Case 5 – 20 s

(c) Case 3 – 40 s

(d) Case 5 – 40 s

(e) Case 3 – 60 s

(f) Case 5 – 60 s

Figure 13. Pressure distribution for the Iso-Q test-articles using a non-uniform pressure distribution (Case 5) – for clarity, the results are compared to Case 3

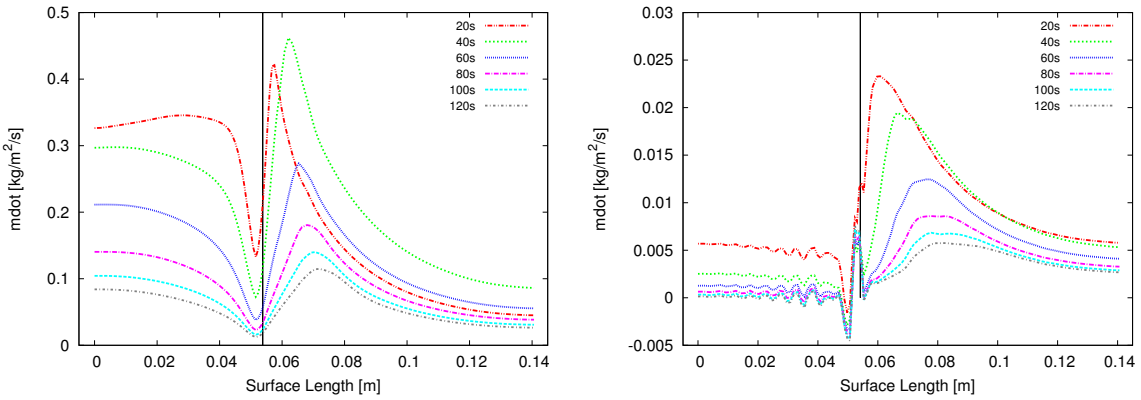

(a) Case 3 (b) Case 5

Figure 14. Surface normal blowing mass flux for Case 5: the black line indicates the separation between the front surface, to the left, and the side surface, to the right – for clarity, the results are compared to Case 3

VII. Acknowledgments

Partial financial support for this work was provided by NASA SBIR Phase-2 Award NNX10CC53P, and NASA Kentucky EPSCoR Award NNX10AV39A. The author would like to thank Dr. Francesco Panerai and Dr. Sean Bailey at the University of Kentucky, as well as Tom van Eeckelen, at LMS Siemens for several useful discussions.

References

[1]Tran, H. K., Johnson, C. E., Rasky, D. J., Hui, F., Hsu, M., Chen, T., Chen, Y., Paragas, D., and L.Kobayashi, "Phenolic Impregnated Carbon Ablators (PICA) as Thermal Protection Systems for Discovery Missions," Tech. Rep. TM-110440, NASA, 1997.

[2]Chen, Y.-K. and Milos, F. S., "Ablation and Thermal Response Program for Spacecraft Heatshield Analysis," *Journal of Spacecraft and Rockets*, Vol. 36, No. 3, May-June 1999, pp. 475–483.
doi:10.2514/2.3469

[3]Martin, A. and Boyd, I. D., "Non-Darcian behavior of pyrolysis gas in a thermal protection system," *Journal of Thermophysics and Heat Transfer*, Vol. 24, No. 1, Jan.-Mar. 2010.
doi:10.2514/1.44103

[4]Moyer, C. B. and Rindal, R. A., "An analysis of the coupled chemically reacting boundary layer and charring ablator. Part 2 - Finite Difference Solution for the In-Depth Response of Charring Materials Considering Surface Chemical and Energy Balances," Contractor Report CR-1061, NASA, 1968.

[5]Chen, Y.-K. and Milos, F. S., "Two-Dimensional Implicit Thermal Response and Ablation Program for Charring Materials," *Journal of Spacecraft and Rockets*, Vol. 38, No. 4, July-August 2001, pp. 473–481.
doi:10.2514/2.3724

[6]Hogan, R. E., Blackwell, B. F., and Cochran, R. J., "Application of Moving Grid Control Volume Finite Element Method to Ablation Problems," *Journal of Thermophysics and Heat Transfer*, Vol. 10, No. 2, April-June 1996.
doi:10.2514/3.789

[7]Milos, F. S. and Chen, Y.-K., "Ablation and Thermal Response Property Model Validation for Phenolic Impregnated Carbon Ablator," *Journal of Spacecraft and Rockets*, Vol. 47, No. 5, 2010, pp. 786–805.
doi:10.2514/1.42949

[8]Marschall, J. and Milos, F. S., "Gas Permeability of Rigid Fibrous Refractory Insulations," *Journal of Thermophysics and Heat Transfer*, Vol. 12, No. 4, October-December 1998, pp. 528–535.
doi:10.2514/2.6372

[9]Covington, M. A., Heinemann, J. M., Goldstein, H. E., Chen, Y.-K., Terrazas-Salinas, I., Balboni, J. A., Olejniczak, J., and Martinez, E. R., "Performance of a Low Density Ablative Heat Shield Material - Erratum," *Journal of Spacecraft and Rockets*, Vol. 45, No. 4, July–August 2008, pp. 854–865.
doi:10.2514/1.40598

[10]Gökçen, T., Chen, Y.-K., Skokova, K. A., and Milos, F. S., "Computational Analysis of Arc-Jet Stagnation Tests Including Ablation and Shape Change," *41st AIAA Thermophysics Conference*, No. AIAA-2009-3596, San Antonio, TX, 22-25 June 2009.
doi:10.2514/6.2009-3596

[11]Milos, F. S. and Chen, Y.-K., "Two-Dimensional Ablation, Thermal Response, and Sizing Program for Pyrolyzing

Ablators," *Journal of Spacecraft and Rockets*, Vol. 46, No. 6, 2009, pp. 1089–1099.
doi:10.2514/1.36575

[12]Chen, Y.-K., Milos, F. S., and Gökçen, T., "Loosely Coupled Simulation for Two-Dimensional Ablation and Shape Change," *40th AIAA Thermophysics Conference*, No. AIAA 2008-3802, Seattle, WA, June 23-26 2008.
doi:10.2514/6.2008-3802

[13]Inman, J. A., Bathel, B. F., Johansen, C. T., Danehy, P. M., Jones, S. B., Gragg, J. G., and Splinter, S. C., "Nitric Oxide PLIF Measurements in the Hypersonic Materials Environmental Test System (HYMETS)," *49th Aerospace Sciences Meeting*, No. AIAA-2011-1090, Orlando, FL, 4-7 January 2011.
doi:10.2514/6.2011-1090

[14]Danehy, P. M., Hires, D. V., Johansen, C. T., Bathel, B. F., Jones, S. B., Gragg, J. G., and Splinter, S. C., "Quantitative Spectral Radiance Measurements in the HYMETS Arc Jet," *50th AIAA Aerospace Sciences Meeting and Exhibit*, No. AIAA-2012-856, Nashville, TN, 7-10 January 2012.
doi:10.2514/6.2012-856

[15]Erzincanli, B., Asma, C. O., and Chazot, O., "Ablative Material Testing at VKI Plasmatron Facility," *10th AIAA/ASME Joint Thermophysics and Heat Transfer Conference*, No. AIAA 2010-4511, Chicago, IL, 28 June - 1 July 2010.
doi:10.2514/6.2010-4511

[16]Vancrayenest, B. and Fletcher, D. G., "Ablation of Carbonaceous Heatshields: Spectroscopic Emission Survey in a Subsonic ICP Flow," *40th AIAA Thermophysics Conference*, No. AIAA 2008-3911, Seattle, WA, 23-26 June 2008 2008.
doi:10.2514/6.2008-3911

[17]Reimer, T., Kuhn, M., Gülhan, A., Esser, B., Sippel, M., and van Foreest, A., "Transpiration Cooling Tests of Porous CMC in Hypersonic Flow," *17th AIAA International Space Planes and Hypersonic Systems and Technologies Conference*, No. AIAA, San Francisco, CA, 11 - 14 April 2011.
doi:10.2514/6.2011-2251

[18]Weng, H., Martin, A., Khan, O. U., and Huai-Bao, Z., "Multi-dimensional modeling of charring ablators," *43rd AIAA Thermophysics Conference*, No. AIAA-2012-2748, New Orleans, LA, June 25-28 2012.
doi:10.2514/6.2012-2748

[19]Zhang, H.-B., Martin, A., and McDonough, J. M., "Parallel Efficiency of the FreeCFD Code for Hypersonic Flows with Chemistry," *24th International Conference on Parallel Computational Fluid Dynamics*, Atlanta, GA, May 21-25 2012.

[20]Darcy, H., *Les Fontaines Publiques de la Ville de Dijon*, Dalmont, Paris, France, 1856.

[21]Lachaud, J., Martin, A., Cozmuta, I., and Laub, B., "Ablation test-case series 1," *4th AFOSR/SNL/NASA Ablation Workshop*, 2010.

[22]van Eekelen, T., Martin, A., Lachaud, J., and Cozmuta, I., "Code and Model Comparisons for the Numerical Simulation of Ablative-material Response: Ablation Test-case Series 3," Poster, Gordon Research Conference on Atmospheric Reentry Physics, Ventura, CA, February 3-8 2013.